ASME Journal of Heat and Mass Transfer
Online journal at:
https://asmedigitalcollection.asme.org/heattransfer

Haochen Sun[1]
College of Aerospace Engineering,
Nanjing University of Aeronautics and Astronautics,
Nanjing 210016, China
e-mail: 1284908358@qq.com

Michael David Atkins
School of Mechanical, Industrial, and Aeronautical Engineering,
University of the Witwatersrand,
Johannesburg 2000, South Africa
e-mail: michael.atkins@wits.ac.za

Kiju Kang
Department of Mechanical Engineering,
Chonnam National University,
Gwangju 61186, South Korea
e-mail: kjkang@chonnam.ac.kr

Tian Jian Lu
College of Aerospace Engineering,
Nanjing University of Aeronautics and Astronautics,
Nanjing 210016, China
e-mail: tjlu@nuaa.edu.cn

Tongbeum Kim[1]
College of Aerospace Engineering,
Nanjing University of Aeronautics and Astronautics,
Nanjing 210016, China
e-mail: tongbeum.kim@nuaa.edu.cn

Extended Neumann's Solution Accounting for Rayleigh–Bénard Convection in the Melt Layer of a Phase Change Material

Neumann's solution has been perceived to be inapplicable for the Stefan problem when Rayleigh–Bénard (R–B) convection exists. Yet, this article challenges this perception by demonstrating the applicability of Neumann's solution in the context of R–B convection. The temporal, countergravitational progression of a liquid–solid interface is distinctively attributed by R–B convection, sequentially transforming from diffusive to convective state as the melt phase thickens. We thus incorporate a lumped parameter, "convective conductivity" that accounts for the distinctive temporal thickening of the melt phase and replaces "stagnant thermal conductivity" in Neumann's solution. Thus, the extended Neumann's solution that includes R–B convection, enables the temporal progression of the liquid–solid interface to be precisely determined for quasi-steady phase transition.
[DOI: 10.1115/1.4065351]

1 Introduction

Phase transition is a key process in thermal energy storage that utilizes latent heat conversion [1]. The charge and discharge of thermal energy occurs during phase transition of a phase change material (PCM) from solid to liquid (melting) and from liquid to solid (solidification), respectively. The temporal and spatial progression of a phase interface determines the total time of the thermal energy storage process. Mathematically, this type of a moving boundary problem referred to as the Stefan problem postulated in 1891 with the only known exact solution of "Neumann's solution," based on the unpublished work by Franz Neumann [2] in 1860 in which the phase transition is initiated and forced particularly by a constant temperature boundary.

Consideration of the melting phase transition as illustrated in Fig. 1(*a*) (bottom), a planar wall boundary at a constant temperature, T_w, drives the liquid–solid phase interface downward ($-y$). Since the constant temperature wall is situated above the PCM, the melting occurs from above and the interface moves along the gravitational axis (g-axis). Initially, the solid PCM is at constant temperature, T_0 and thereafter the heated wall at constant temperature (T_w) causes the melting of the solid phase. The temporal progression of the phase interface can be analytically expressed by Neumann's solution, separately in the dimensional and dimensionless forms [5]

$$S(t) = 2\lambda\sqrt{\frac{k_l t}{\rho_l c_{pl}}} \tag{1a}$$

$$\xi(\tau) = 2\lambda\sqrt{\tau} \tag{1b}$$

where $\xi = S(t)/H$ and $\tau = \alpha_l t/H^2$ are the dimensionless melt thickness and time, respectively, H is the total thickness along the y-axis of a given PCM, λ is the positive root of the transcendental equation

$$\frac{\exp(-\lambda^2)}{\mathrm{erf}(\lambda)} + \frac{N_k}{\sqrt{N_\alpha}}\frac{(T_m - T_0)}{(T_m - T_w)}\frac{\exp\left(-\frac{\lambda^2}{N_\alpha}\right)}{\mathrm{erfc}\left(\frac{\lambda}{\sqrt{N_\alpha}}\right)} = \frac{\lambda\sqrt{\pi}}{\mathrm{Ste}} \tag{2}$$

Here, N_k and N_α are the solid-to-liquid ratios of thermal conductivity (k_s/k_l) and diffusivity (α_s/α_l), respectively, $\alpha = k/\rho c_p$ is the thermal

[1]Corresponding author.

Contributed by the Heat Transfer Division of ASME for publication in the Journal of Heat and Mass Transfer. Manuscript received January 6, 2024; final manuscript received March 20, 2024; published online May 6, 2024. Assoc. Editor: Sandra Boetcher.

diffusivity with k, ρ, and c_p being the thermal conductivity, density, and thermal capacity, separately. The subscripts, s and l denote the solid and liquid phases of a phase change material. Ste is the Stefan number that quantifies the ratio of sensible heat-to-latent heat, defined as $\text{Ste} = c_{pl}(T_w - T_m)/L_h$, where T_m is the phase-change (or melting) temperature and L_h is the latent heat.

Neumann's solution (Eq. (1)) has been known to precisely predict the phase interface location as a function of time, which traverses away from an isothermal boundary as depicted in Fig. 1(*a*) (bottom). Immediately after the onset of phase transition, the phase interface moves at a high rate and then the progression rate decreases steeply, eventually until full melting or solidification (see Fig. 1(*b*)). As further indicated in Fig. 1(*b*), the Stefan number that measures the driving magnitude determines a specific rate of phase transition.

Now, we consider phase transition initiated and driven by the isothermal boundary of T_w against the gravitational axis, where typically the constant temperature wall is situated *below* the phase change material, as shown in Fig. 1(*a*) (top) and the phase interface moves upward ($+y$). Initially, a planar liquid–solid interface forms. Within a melt layer, a continuous density gradient exists, driving convective flow and forming a counter-rotating vortical structure—convection cells with discrete cold and hot plumes. As the melt layer becomes thicker, the initial planar phase interface transforms into a wavy pattern. The schematic illustration in Fig. 1(*a*) (top) shows that hot plumes rise and bifurcate horizontally after stagnation on the phase interface. The horizontally drifted hot plumes collide with those from neighboring plumes, forming cusps where cold plumes develop and sink. As a result, the large convection cells are formed with either cusp-to-cusp or bifurcation-to-bifurcation spacing configuring a unit cell of such vortical structures. The counter-rotating vortices are almost symmetrical with respect to both cusp and bifurcation points with the head-on collision at the cusp point, leading to destabilization of the vortices [6]. In particular, cold plumes are generated by the collision of two boundary layers developed from the phase interface descending, leading to the formation of a high curvature cusp sustained by the continuous supply of cold fluid descending. This natural convective phenomenon is conventionally termed "Rayleigh–Bénard (R–B) convection."

With R–B convection, the liquid–solid interface, often termed a "melting front" moves upward against the gravitational axis away from the isothermal (bottom) planar surface. When the melting is caused due to the constant temperature wall heating the PCM from below, the melting front initially follows Neumann's solution (Fig. 1(*b*)) for $\tau < \tau_1$. However, after a certain period greater than, i.e., $\tau > \tau_1$, the upward movement of the melting front suddenly accelerates due to strengthening R–B convection. Thus, the melting front progresses faster than the predicted rate by Neumann's solution [3,7–10]. Here, the deviation σ between the experimental melting front and Neumann's solution increases, which demonstrates the inapplicability of Neumann's solution when there is R–B convection. The deviation becomes substantial as the phase transition progresses further. The extent of such acceleration (or deviation) depends on phase change material's properties and Stefan number [8].

Several analytical studies were conducted to grasp the underlining physics of the phase transition behavior that was experimentally observed [3,7–10]. Boger and Westwater [7] investigated the phase interface velocity by solving the energy balance equation via a numerical discretization scheme with assumed temperature distributions in both liquid and solid phases. However, they could not predict the interfacial velocity with R–B convection from the onset of melting since their method required the co-existence of both liquid and solid phases. A series of notable subsequent works by Hale and Viskanta [9] and Gau and Viskanta [3,10] also solved the energy balance equation via a numerical scheme to predict the temporal progression of a liquid–solid interface. However, due to the nonlinearity associated with the moving boundary, the energy balance equation could not be in a closed form. Therefore, the solution was approximated by the integration method [3] whose results are included in Fig. 1(*b*) where the melting front movement is upward. In summary, the approximate analytical solutions for the temporal phase transition based on the energy balance equation can offer arguably good agreement for R–B convection [3,9].

In addition to the analytical approaches, numerical simulation schemes have also been employed, such as finite element method [11], finite volume method [4,12–15] (e.g., OpenFOAM [4,13] and ANSYS FLUENT [14,15]). These works have predicted the phase transition process focusing particularly on (i) phase transition in a finite enclosure [4,11–15]; (ii) distinctive phase transition regimes [4,13]; and (iii) parametric effects of enclosures [14] and Prandtl number [15]. The numerical data were compiled into correlations [15] based on the transition time (t) and melt thickness ($S(t)$), yet the physical interplay among relevant geometric and thermophysical parameters were concealed.

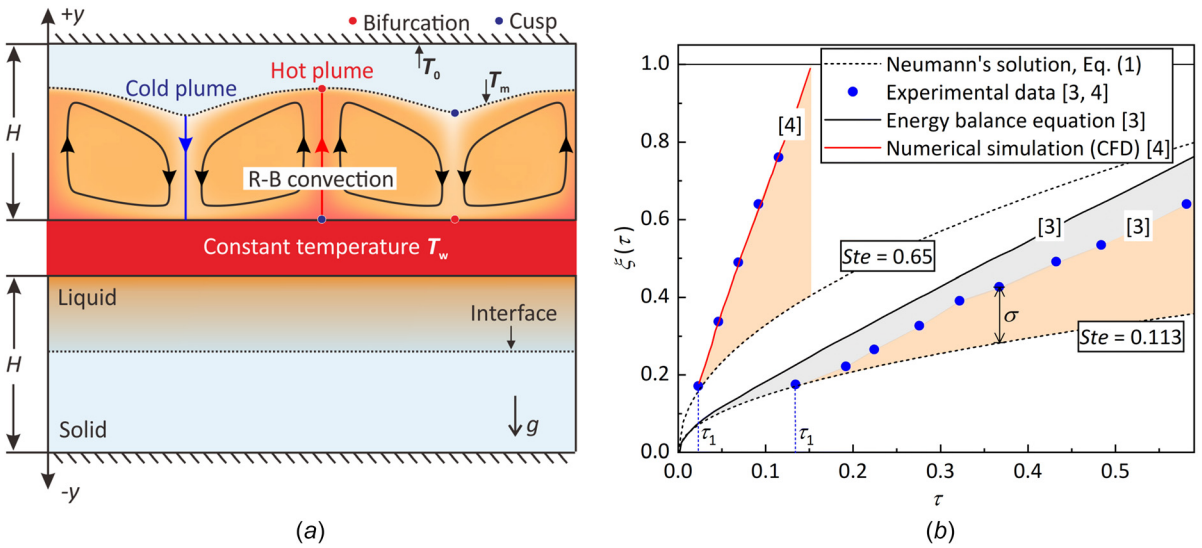

Fig. 1 Stefan problem without and with R–B convection. (*a*) Schematic of phase transition from solid to liquid with respect to the gravitational axis. (*b*) Solving Stefan problem with Rayleigh–Bénard (R–B) convection with comparisons between experimental data and energy balance equation for Ste = 0.113 where σ denotes the deviation between the experimental data [3] and Neumann's solution and between experimental and numerical simulation data for Ste = 0.65 [4].

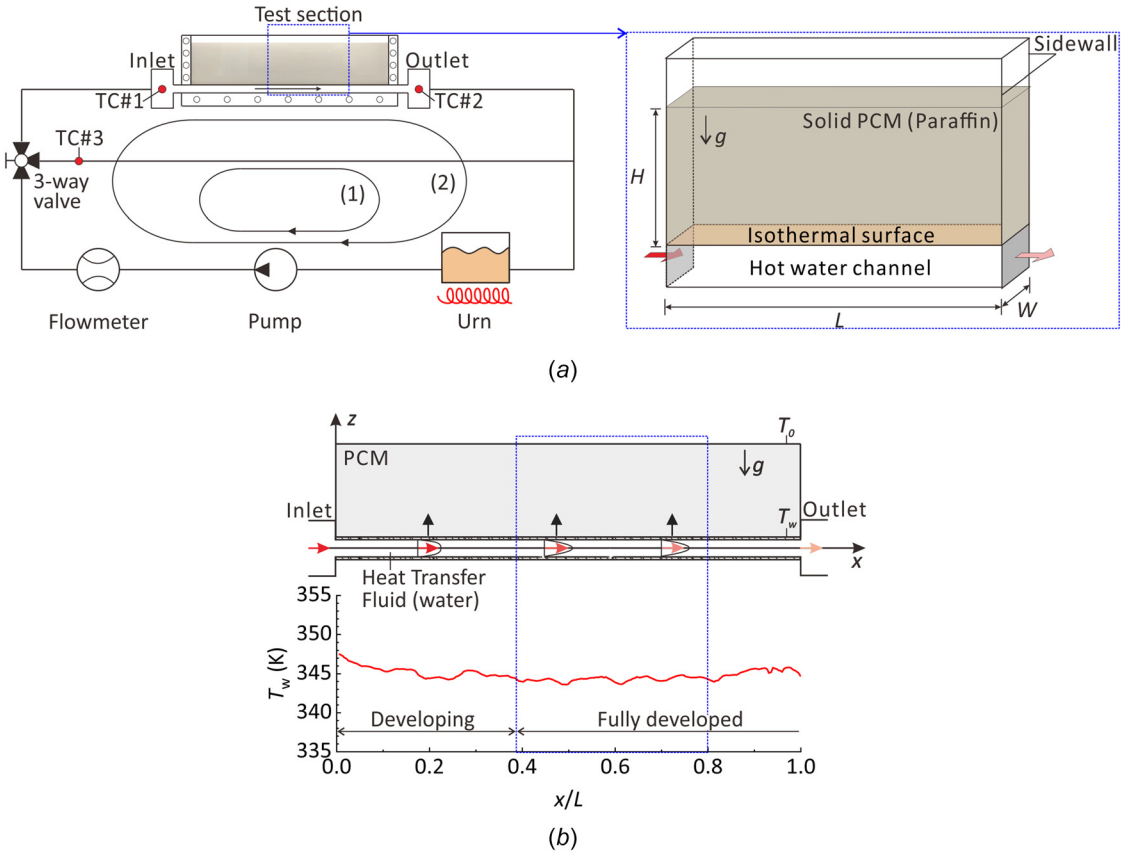

Fig. 2 Experimental setup. (*a*) A water circulation system with a test section (narrow rectangular enclosure). (*b*) Wall temperature (T_w) distribution along the rectangular hot water channel surface measured by an infrared (IR) camera at $Re_{Dh} = 230$.

Table 1 Details of the test apparatus (or sensor)

Apparatus (or sensor)	Manufacturer	Uncertainty/resolution
Thermostatic water tank	Changzhou Yuexin Instrument Manufacturing Co., Changzhou, Ltd., China	±0.70% in uniformity
Pump	Chengdu Haixun Fluid Technology Co., Ltd., Chengdu, China	N/A
Volume flowrate meter	Zhongjiang Energy Saving Electronics Co., Ltd., Foshan, China	±1.00% full scale
Three-way valve	Shanghai Lelong Valve Co., Ltd., Shanghai, China	N/A
T-type thermocouples	OMEGA Engineering (TTSS-116G-2), Norwalk, USA	±1.0 °C

The exact solutions provide physical insights into the mechanisms of phase transition and the melting front propagation albeit acceptable prediction accuracy can be obtained from well-defined full-scale numerical calculations including computational fluid dynamics (CFD). However, the inapplicability of Neumann's solution to the Stefan problem with the presence of any apparent convective flow within the melt layer such as R–B convection has been widely perceived [16]. Thus, alternative methods were implemented such as solving the energy balance equation via numerical schemes and CFD programs. In this article, we challenge the perception by demonstrating the applicability of Neumann's solution with R–B convection, created by the isothermal (constant temperature) wall situated below the phase change material. To this end, we extend the original Neumann's solution by introducing a lumped parameter, "convective conductivity" that reflects the distinctive temporal thickening of the melt layer due to convection and implicitly replaces "stagnant thermal" conductivity for the assumed quasi-steady-state phase transition.

2 Experimental Details

2.1 Test Rig and Measurement Setup. To visualize and quantify the temporal progression of a liquid–solid interface, a purposely built test rig was used as shown in Fig. 2. The test rig consisted of a thermostatic water tank (urn), pump, flowmeter, three-way valve, thermocouples, and a test section as illustrated in Fig. 2(*a*), with the manufacturer and uncertainty details given in Table 1. The total volume of the 2 kW thermostatic water tank was 27 l with an operating temperature range from 25 °C up to 100 °C. The water circulation was implemented by a radial pump. Downstream of which, a turbine flowmeter equipped with a Hall effect sensor was connected with the operating range of 0.03–0.15 L/min and maximum operating pressure and temperature being 1.75 MPa and 85 °C (358.15 K), respectively. A three-way automatic ball valve controlled the water circulation route denoted as (1) and (2) in Fig. 2(*a*). To monitor water temperatures, three T-type thermocouples (TC#1, TC#2, and TC#3) were connected to a data acquisition system (Keysight Technologies 34972 A module).

The test section was an enclosure for the PCM, e.g., paraffin wax, made of 10 mm thick transparent acrylic sheets for optical access. The length L and width W of the rectangular enclosure were 280 mm and 8 mm, respectively, with the depth of $H = 50$ mm (Fig. 2(*a*)). A thin-walled square stainless-steel channel with 0.05 mm thickness was placed at the bottom of the enclosure to provide an isothermal boundary condition, by the temperature-controlled hot water flow in the channel (see Fig. 2(*a*)).

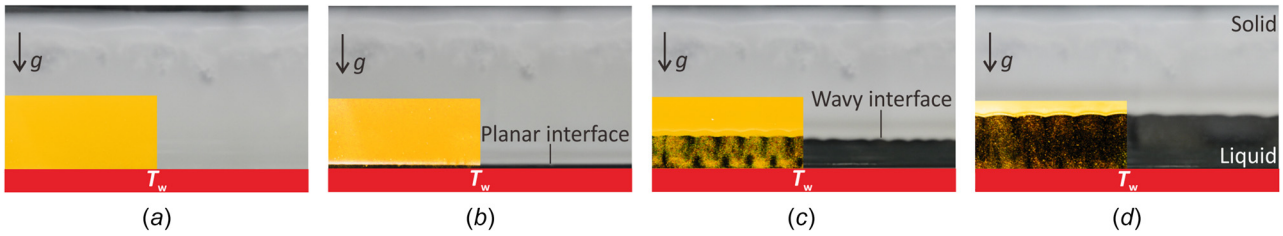

Fig. 3 Experimental melting process showing visualized phase transition. (*a*) $t_0 = 0$ s, (*b*) $t_1 = 50$ s (with a planar phase interface), (*c*) $t_2 = 300$ s (with a wavy phase interface), and (*d*) $t_3 = 650$ s.

The temperature of water in the urn was set at 75 °C (348.15 K). After it reached the set value, the pump began to circulate hot water through a closed route (1) in Fig. 2(*a*). The volume flowrate was set to be 0.048 L/min to make the mean flow velocity in the channel of the test section reach 0.013 m/s, which corresponded to the Reynolds number of $\mathrm{Re}_{Dh} = 230$, defined as, $\mathrm{Re}_{Dh} = \rho U_m D_h/\mu$, where ρ and μ are the density and dynamic viscosity of the heat transfer fluid (hot water), U_m is the mean velocity and $D_h = 7.9$ mm, is the hydraulic diameter of the hot water (square stainless-steel) channel. When the water temperature measured by TC#3 in (1) reached the set value, the three-way valve switched the water circulation route to (2) and subsequently hot water entered circuit (2). Thus, phase transition of the paraffin wax was initiated. The two thermocouples (TC#1 and TC#2) measured the temperatures of hot water at both inlet and outlet of the hot water channel.

An infrared (IR) camera was used to measure the surface temperature along the hot water channel. The outer side of the rectangular stainless-steel channel located below the enclosure was coated with a thin layer of "matte black" paint with high emissivity, thereby improving the accuracy of temperature measurement [17]. The emissivity (ε) of the IR camera was set according to measurement of local temperatures on the channel surface using T-Type thermocouples, where the IR camera emissivity ($\varepsilon = 0.98$) was adjusted iteratively to ensure the IR camera temperature matches the thermocouple measurement. The surface temperature distribution along the x-axis (Fig. 2(*b*)) shows that at $x/L = 0$ the temperature was about 74.4 °C (347.55 K), decreasing to 71.5 °C (344.65 K). At the inlet of the channel, the water flow underwent its development (developing flow regime) until its full development (fully developed flow regime) as convecting further downstream. The water flow was laminar. Thus, the length of the developing regime was estimated to be $L_e = 0.06\mathrm{Re}_{Dh}D_h \sim 0.109$ m, which corresponded to $L_e/L \sim 0.39$. As consistently shown by the measured temperature data, the surface temperature decreased from the inlet until $x/L = 0.39$. After which, the hot water channel's surface temperature became uniform being 71.5 °C (344.65 K) as indicated in Fig. 2(*b*). Therefore, our visual measurement was carried out at $x/L = 0.39$–0.8 where fully developed hot water flow transferred heat to the rectangular enclosure, so in the following studies, constant temperature wall is at 71.5 °C (344.65 K). After $x/L = 0.8$, the surface temperature was observed to increase slightly near the outlet.

2.2 Image Processing. A digital camera mounted on a tripod was placed perpendicular to the transparent sidewall of the rectangular enclosure to capture a series of still images of the paraffin wax being melt from the bottom. Images were taken every 5 s for 18.3 min (1100 s). Thus, in total, 210 still images were stored. Figure 3 shows the experimental melting process with visualized phase transition at $t_0 = 0$ s, $t_1 = 50$ s, $t_2 = 300$ s, $t_4 = 650$ s.

Using an image process software, the position of a liquid–solid interface along the z-axis (Fig. 4(*a*)) was determined. After the onset of phase transition, the liquid–solid interface were planar. As the melt layer thickened, the initial planar phase interface transformed into a wavy pattern as depicted in Fig. 4(*b*). The lowest position $S'_{\min}$ from the bottom surface corresponded to the cusp and the highest position $S'_{\max}$ corresponded to the bifurcation.

As seen from the side view (y–z plane), the actual highest position of the melt front existed at the central width ($W/2$) resulting from the three-dimensional nature of R–B convection illustrated in Fig. 4(*a*) and possible heat loss through the side walls. This region marked in gray in the y–z plane underestimated the location of the melting as much as δ being estimated via the postimage process based on the images taken in the y–z plane. Thus, the actual mean melt thickness was corrected and calculated by $S = (S'_{\min} + S'_{\max})/2 + \delta$. The mapping of the melt thickness propagation was determined via calibration of the digital camera images pixel dimensions to the physical dimensions of the test enclosure. For example, the bolt hole centers used to seal the Perspex sheets of the enclosure were employed to determine the scaling factor (233.6±5 μm/pixel) between the object and the images plane.

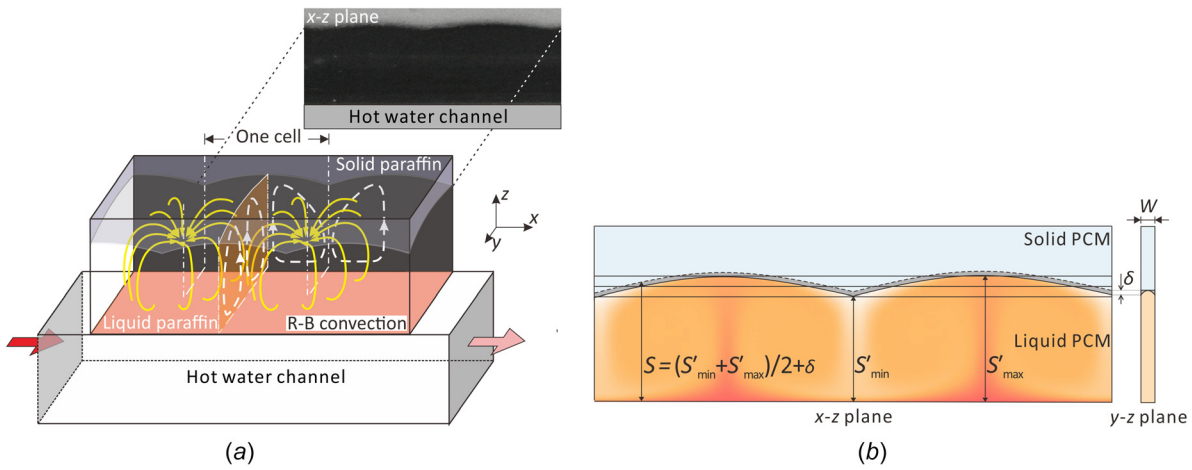

Fig. 4 Image process for estimating the temporal progression of a liquid–solid interface. (*a*) 3D R–B convection diagram and *x–z* plane experimental visualization. (*b*) Schematics for R–B convection with shaded area.

Table 2 Thermophysical properties (water at 289.15 K, solid paraffin wax at 310.65 K, liquid paraffin wax at 333.15 K)

Properties	Water	Paraffin wax, CAS: 8002-74-2	Uncertainty	Typical range of paraffin
T_m (K)	273.15	323.65	±1.00%	323.15–343.15
L_h (J/kg)	N/A	204,550	±1.00%	168,000–180,000 [18,19]
c_{pl} (J/kg K)	4060.126	4751	±1.00%	2100–2150 [18,19]
c_{ps} (J/kg K)	N/A	3367	±1.00%	2000 [19]
ρ_l (kg/m^3)	998.97	841	±0.12%	760–840 [18,19]
ρ_s (kg/m^3)	N/A	881	±0.12%	880–910 [18,19]
k_l (W/m K)	0.58	0.825	±3.00%	0.2 [18,20]
k_s (W/m K)	N/A	0.338	±3.00%	0.24 [18]
μ (Pa·s)	0.0010989	0.0051	±3.00%	0.005–0.204 [18,21–25]
β_l (1/K)	0.000143	0.000364	±0.10%	0.00011–0.00061 [18,19]

Table 3 Errors of measured parameters

Parameters	Error
Liquid–solid interface location refers to $S(t)$	$\Delta S(t) = \pm 0.6$ mm
Total melt thickness refers to H	$\Delta H = \pm 0.6$ mm
Infrared camera temperature refers to T_w	$\Delta T_w = \pm 0.1$ °C

2.3 Thermophysical Properties of Phase-Change Material. A paraffin wax was employed as a phase-change material in this study. Prior to measurements, thermophysical parameters of both water and paraffin wax were quantified at ambient conditions and assumed to be constant in the analysis. Relevant thermophysical parameters include melting temperature (T_m), latent heat (L_h), heat capacity (c_p), density (ρ), thermal conductivity (k), dynamic viscosity (μ), and the coefficient of thermal expansion (β).

The melting temperature, latent heat, and heat capacity were measured using a thermal gravimetric analyzer and a differential scanning calorimetry by TGA/DSC 3+ (METTLER TOLEDO, Shanghai, China). The uncertainties were within ±1% for respective parameters. The density was measured using a gradient density meter, DGA3/DGA6 (Ray Ran, Birmingham, UK). The instrument used a linear displacement transducer to calibrate the density gradient of the column of a specimen. The associated uncertainty was reported to be ±0.12%. The thermal conductivity was quantified using a laser thermal conductivity analyzer, LFA457 (NETZSCH, Selb, Germany). Based on one-dimensional thermal conduction, an infrared detector continuously measured the temperature rise at the center of a specimen surface. A correlation curve between temperature rise (detector signal) and time was obtained by measuring the half heating time, $t_{1/2}$ (defined as time taken for the surface temperature of the specimen to rise to half its maximum value after receiving the light pulse irradiation). The uncertainty was reported to be ±3%. The dynamic viscosity was measured using a viscometer (Ubbelohde) that calculated time for a liquid of interest flowing out of the capillary viscometer with the associated uncertainty being ±3%. The coefficient of thermal expansion was characterized by means of a thermal dilatometer (PZY vertical thermal dilatometer). The uncertainty was reported to be ±0.1%. The measured thermophysical properties of the paraffin wax used in this study are listed in Table 2 where l and s denote liquid and solid phase, respectively.

2.4 Measurement Uncertainties. Error and uncertainty associated with relevant parameters, liquid–solid interface position ($S(t)$), total melt thickness (H), infrared camera temperature (T_w), and thermal physical properties (T_m, L_h, c_p, ρ, and k) were estimated as follows. The root sum square method [26] was employed for estimating errors. If $y = f(x_1, x_2, \ldots, x_n)$, then the error propagated by x_i in the variable, y is given by

$$\Delta y = \sqrt{\left(\frac{\partial y}{\partial x_1}\Delta x_1\right)^2 + \left(\frac{\partial y}{\partial x_2}\Delta x_2\right)^2 + \cdots + \left(\frac{\partial y}{\partial x_n}\Delta x_n\right)^2} \quad (3)$$

where Δx_i is the error (absolute uncertainty) in x_i. Based on Eq. (3), the error of Stefan number, dimensionless melt thickness and time were separately estimated as follows:

For Stefan number ($\mathrm{Ste} = c_{pl}(T_w - T_m)/L_h$), ΔSte can be calculated as

$$\Delta \mathrm{Ste} = \sqrt{\left(\frac{\partial \mathrm{Ste}}{\partial c_{pl}}\Delta c_{pl}\right)^2 + \left(\frac{\partial \mathrm{Ste}}{\partial T_w}\Delta T_w\right)^2 + \left(\frac{\partial \mathrm{Ste}}{\partial T_m}\Delta T_m\right)^2 + \left(\frac{\partial \mathrm{Ste}}{\partial L_h}\Delta L_h\right)^2} \quad (4)$$

where $\frac{\partial \mathrm{Ste}}{\partial c_{pl}} = \frac{T_w - T_m}{L_h}$, $\frac{\partial \mathrm{Ste}}{\partial T_w} = \frac{c_{pl}}{L_h}$, $\frac{\partial \mathrm{Ste}}{\partial T_m} = -\frac{c_{pl}}{L_h}$, and $\frac{\partial \mathrm{Ste}}{\partial L_h} = -\frac{c_{pl}(T_w - T_m)}{L_h^2}$ to be $\Delta \mathrm{Ste} = \pm 0.0138$ based on the errors in Tables 2 and 3. Therefore, the uncertainty of Stefan number (Ste) was calculated to be ±2.83%.

For dimensionless melt thickness ($\xi = S(t)/H$), $\Delta\xi$ can be calculated as

$$\Delta \xi = \sqrt{\left(\frac{\partial \xi}{\partial S(t)}\Delta S(t)\right)^2 + \left(\frac{\partial \xi}{\partial H}\Delta H\right)^2} \quad (5)$$

where $\frac{\partial \xi}{\partial S(t)} = \frac{1}{H}$ and $\frac{\partial \xi}{\partial H} = -\frac{S(t)}{H^2}$ which is related to the melt thickness, $S(t)$. $\Delta\xi$ was estimated to be within ±0.0283 based on the errors in Table 3. Therefore, the relative uncertainty of dimensionless melt thickness (ξ) was estimated to be within ±60.82%. At the beginning of melting, the dimensionless melt thickness is small causing a large uncertainty (~±60.82%). On the other hand, as the melt layer thickens, the uncertainty becomes substantially reduced to ±2.83%.

For dimensionless melt time ($\tau = k_l t/\rho_l c_{pl} H^2$), $\Delta\tau$ can be calculated as

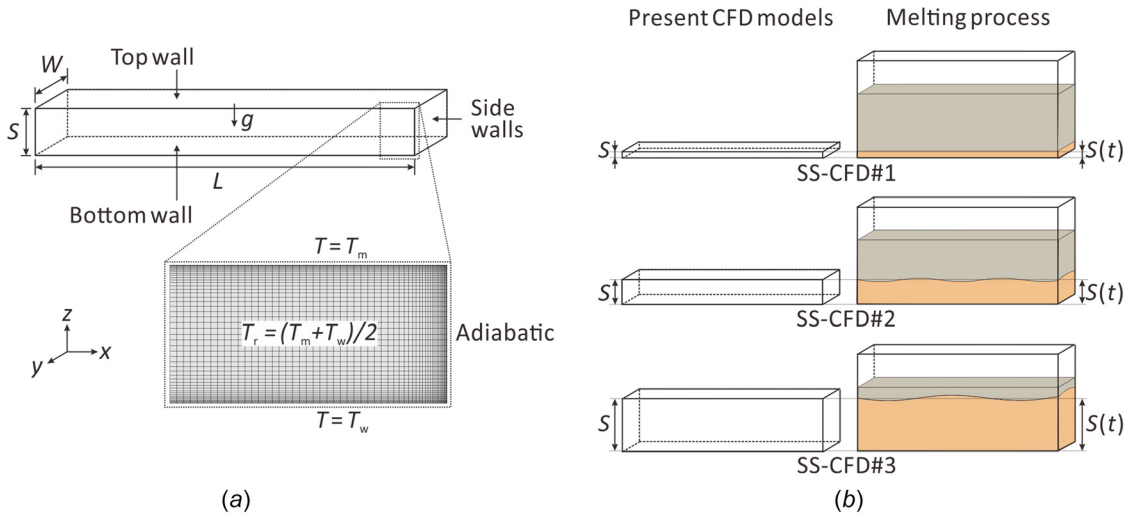

Fig. 5 CFD models. (*a*) Geometry of the computational domain for the rectangular enclosure. (*b*) The idealization of the melted phase thickness (*S*) for a sequence of steady-state (SS) CFD simulations, compared to the quasi-steady melting process where the melt layer thickness *S*(*t*) varies with time.

$$\Delta\tau = \sqrt{\left(\frac{\partial\tau}{\partial k_l}\Delta k_l\right)^2 + \left(\frac{\partial\tau}{\partial \rho_l}\Delta\rho_l\right)^2 + \left(\frac{\partial\tau}{\partial c_{pl}}\Delta c_{pl}\right)^2 + \left(\frac{\partial\tau}{\partial H}\Delta H\right)^2} \tag{6}$$

where $\frac{\partial\tau}{\partial k_l} = \frac{t}{\rho_l c_{pl} H^2}$, $\frac{\partial\tau}{\partial \rho_l} = -\frac{k_l t}{\rho_l^2 c_{pl} H^2}$, $\frac{\partial\tau}{\partial c_{pl}} = -\frac{k_l t}{\rho_l c_{pl}^2 H^2}$, and $\frac{\partial\tau}{\partial H} = -\frac{2k_l t}{\rho_l c_{pl} H^3}$ which is related to the melt time, t. $\Delta\tau$ was estimated to be within ± 0.0129 based on the errors in Tables 2 and 3. The uncertainty of dimensionless melt time (τ) was estimated to be within $\pm 5.10\%$.

3 Numerical Details

3.1 Problem Statement. A series of numerical simulations were performed to obtain the relationship between convective heat transfer coefficient h_c and melt thickness $S(t)$, that are independent of the present experimental data. The simulations applied a constant wall temperature at the bottom wall to the melted phase to induce Rayleigh–Bénard convection. The computational domain for a rectangular enclosure of length of L and width of W that was heated from below is shown in Fig. 5(*a*). Based on the quasi-steady-state assumption for the melt-front progression, a sequence of discrete steady-state CFD simulations were performed. Here, the melt layer thickness (S) of the PCM was kept constant in each simulation run as shown in Fig. 5(*b*). To determine the relationship between the convective heat transfer coefficient (h_c) and the thickness (S), subsequent steady-state CFD simulations increased the melt layer thickness (S); SS-CFD#1, SS-CFD#2, and SS-CFD#3, thereby approximating of the melt layer thickness $S(t)$ changes during the melting process (Fig. 5(*b*)). The direction of the gravitational acceleration (g) is opposite to the z-axis.

3.2 Governing Equations. All transport properties (e.g., melting temperature (T_m), latent heat (L_h), heat capacity (c_p), density (ρ), thermal conductivity (k), dynamic viscosity (μ), and the coefficient of thermal expansion (β)) were assumed to be constant in the momentum equations except for the buoyancy term, which was linearized—the Boussinesq fluid. The governing equations for the Boussinesq fluid [27] are given as:

(a) Continuity equation

$$\frac{\partial u}{\partial x} + \frac{\partial v}{\partial y} + \frac{\partial w}{\partial z} = 0 \tag{7}$$

(b) Momentum equations

$$\rho_l\left(\frac{\partial u}{\partial t} + u\frac{\partial u}{\partial x} + v\frac{\partial u}{\partial y} + w\frac{\partial u}{\partial z}\right) = -\frac{\partial p}{\partial x} + \mu\left(\frac{\partial^2 u}{\partial x^2} + \frac{\partial^2 u}{\partial y^2} + \frac{\partial^2 u}{\partial z^2}\right) \tag{8}$$

$$\rho_l\left(\frac{\partial v}{\partial t} + u\frac{\partial v}{\partial x} + v\frac{\partial v}{\partial y} + w\frac{\partial v}{\partial z}\right) = -\frac{\partial p}{\partial y} + \mu\left(\frac{\partial^2 v}{\partial x^2} + \frac{\partial^2 v}{\partial y^2} + \frac{\partial^2 v}{\partial z^2}\right) \tag{9}$$

$$\rho_l\left(\frac{\partial w}{\partial t} + u\frac{\partial w}{\partial x} + v\frac{\partial w}{\partial y} + w\frac{\partial w}{\partial z}\right) = -\frac{\partial p}{\partial z} + \mu\left(\frac{\partial^2 w}{\partial x^2} + \frac{\partial^2 w}{\partial y^2} + \frac{\partial^2 w}{\partial z^2}\right) + \rho_l g\beta(T - T_r) \tag{10}$$

(c) Energy equation

$$\rho_l c_{pl}\left(\frac{\partial T}{\partial t} + u\frac{\partial T}{\partial x} + v\frac{\partial T}{\partial y} + w\frac{\partial T}{\partial z}\right) = k_l\left(\frac{\partial^2 T}{\partial x^2} + \frac{\partial^2 T}{\partial y^2} + \frac{\partial^2 T}{\partial z^2}\right) \tag{11}$$

where μ, c_{pl}, k_l, and ρ_l are the dynamic viscosity, thermal capacity, thermal conductivity, and density of the liquid phase, respectively, and $T_r = (T_w + T_m)/2$ is the reference temperature.

3.3 Boundary Conditions. The boundary conditions at each wall (Fig. 5) in a dimensionless form are prescribed as follows:

(a) Bottom wall

$$u = v = w = 0, \quad T = T_w \quad \text{at} \quad z = 0; \quad 0 \le x \le L; \quad 0 \le y \le W \tag{12a}$$

(b) Top wall

$$u = v = w = 0, \quad T = T_m \quad \text{at} \quad z = S; \quad 0 \le x \le L; \quad 0 \le y \le W \tag{12b}$$

(c) Side walls

$$u = v = w = 0, \quad \frac{\partial T}{\partial x} = 0 \text{ at } x = 0, L; \quad 0 \le y \le W; \quad 0 \le z \le S \tag{13a}$$

$$u = v = w = 0, \quad \frac{\partial T}{\partial y} = 0 \quad \text{at} \quad y = 0, W; \quad 0 \le x \le L; \quad 0 \le z \le S \tag{13b}$$

The top and bottom walls are all under constant temperature boundary conditions (Eq. (12)). The top wall temperature was set at the melting temperature while the bottom wall temperature was at the heating temperature. Four side walls were set to be adiabatic (Eq. (13)) as shown in Fig. 5. Initially, the PCM is at a constant temperature, T_0.

3.4 Numerical Scheme. A commercial software, ANSYS FLUENT 2020 R2 was used with the finite volume method. To solve the discrete form of the conservation equations, a coupling algorithm for the velocity and pressure fields was used to the PRESTO! (PREssure STaggering Option) scheme for the pressure term. The convection terms of Eqs. (8)–(10) were discretized using the second-order upwind scheme. The relaxation factors for pressure, momentum, density, volumetric force, and energy were 0.5, 0.5, 0.5, 0.5, and 0.75, respectively. The convergence criterion was set where scale residuals of the continuity equation were less than 10^{-7}, the momentum equations were less than 10^{-7}, and the energy equation was less than 10^{-7}.

3.5 Grid Independence and Experimental Validation. The numerical simulations investigated how differing melt thickness $S(t)$ affects the convective heat transfer coefficient h_c, which was accomplished by varying the fluid domain height of the melted phase. The domain discretization had a fixed node density (the number of elements in the z-axis divided by the melt thickness in the z-axis) and an inflation layer was implemented on each side of the walls with the cell growth rate of 1.1. The parameters of distilled water (289.15 K) [28] and paraffin (333.15 K) used for experimental validation are given in Table 3.

The experimental validation and grid independence analysis were based on the comparison with the experimental results for distilled water at the reference temperature of $T_r = 16\,^{\circ}\text{C}$ (289.15 K) [28]. The tested grid numbers were 190,608, 401,128, 796,290, and 1,356,030 with the corresponding grid sizes of $152 \times 57 \times 22$, $203 \times 76 \times 26$, $254 \times 95 \times 33$, and $305 \times 114 \times 39$, respectively. Figure 6 shows the convergence for the case of $\Delta T = T_w - T_m = 1.46$ K. With the cell number of 190,608 (i), the total heat flux of the simulation results deviates significantly from the experimental value, from (ii) to (iv), the total heat flux value remains unchanged, being in good agreement with the experimental data [28]. Therefore, the grid density equal to the grid size of $203 \times 76 \times 26$ was adopted for subsequent numerical simulations.

To validate the present numerical setup, three differing ΔT values were compared with the results of a previous study [28] in Fig. 6. The simulation results are in good agreement ($-2.24\% \sim +2.86\%$) with the experimental data. After validation, paraffin wax was used as the working fluid, replacing distilled water to obtain the relationship between the convective heat transfer coefficient h_c and the thickness S of the melt layer. The paraffin wax was initially at a constant temperature of $T_0 = 25\,^{\circ}\text{C}$ (298.15 K). The top wall temperature was set at the melting temperature of $T_m = 50.5\,^{\circ}\text{C}$ (323.65 K) while the bottom wall temperature was at the isothermal wall temperature of $T_w = 71.5\,^{\circ}\text{C}$ (344.65 K).

4 Results and Discussion

4.1 The Implicit, Semi-Analytical Extension. We aimed to implicitly and semi-analytically extend Neumann's solution to estimate the temporal progression of a liquid–solid interface with the presence of laminar R–B convection [29] in the melt layer. The key idea was conceptualized based on prior observations [6,30,31] as follows. In steady-state natural convection, the heat transfer varies with the depth (or thickness) of a liquid layer. However, the variation has two distinctive characteristics as (i) heat transfer through a very thin liquid layer is dominated by "diffusion" and (ii) heat transfer across the thickened liquid layer is increased by large scale counter-rotating vortices (i.e., R–B convection), indicating the dominance of "advection."

For a typical PCM in thermal energy storage applications, e.g., paraffin, phase transition occurs *quasi-steadily* due to intrinsically low stagnant thermal conductivity [32]. Despite the melt front progression varying with time, the movement is also slow enough for it to be analyzed as a sequence of steady-state processes, whereby the convective heat transfer from the R–B cells, behaves similarly to a steady-state melted layer of thickness (S). Hence, we incorporated a lumped parameter that accounted for heat transfer across the melt (or liquid) layer solely via equivalent conduction, newly termed

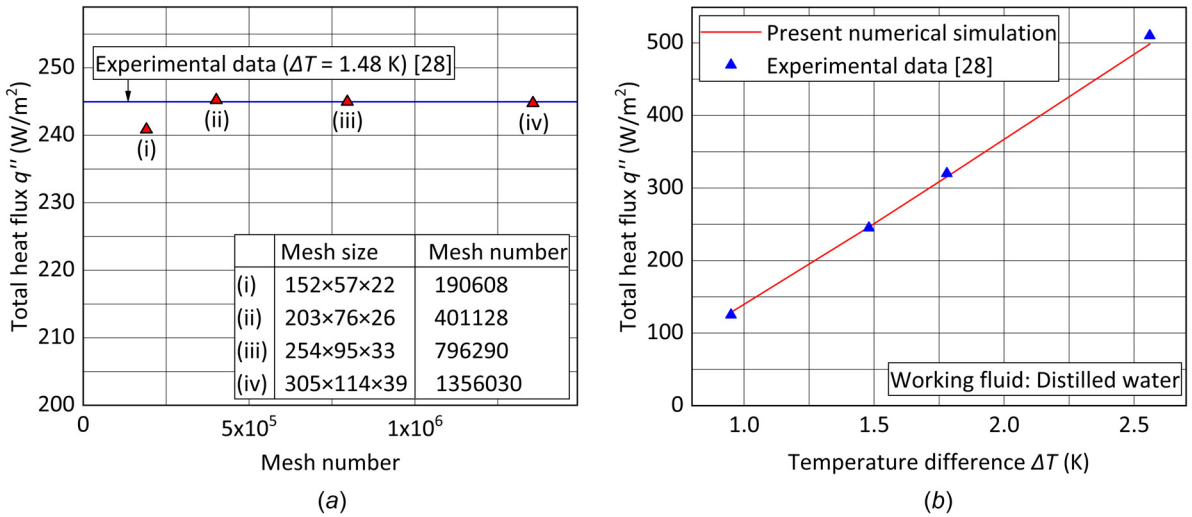

Fig. 6 Grid independence and experimental validation. (*a*) Grid independence for $\Delta T = T_w - T_m = 1.46$ K. (*b*) Experimental validation with Ref. [28] for total heat flux changing with temperature difference ($\Delta T = T_w - T_m$).

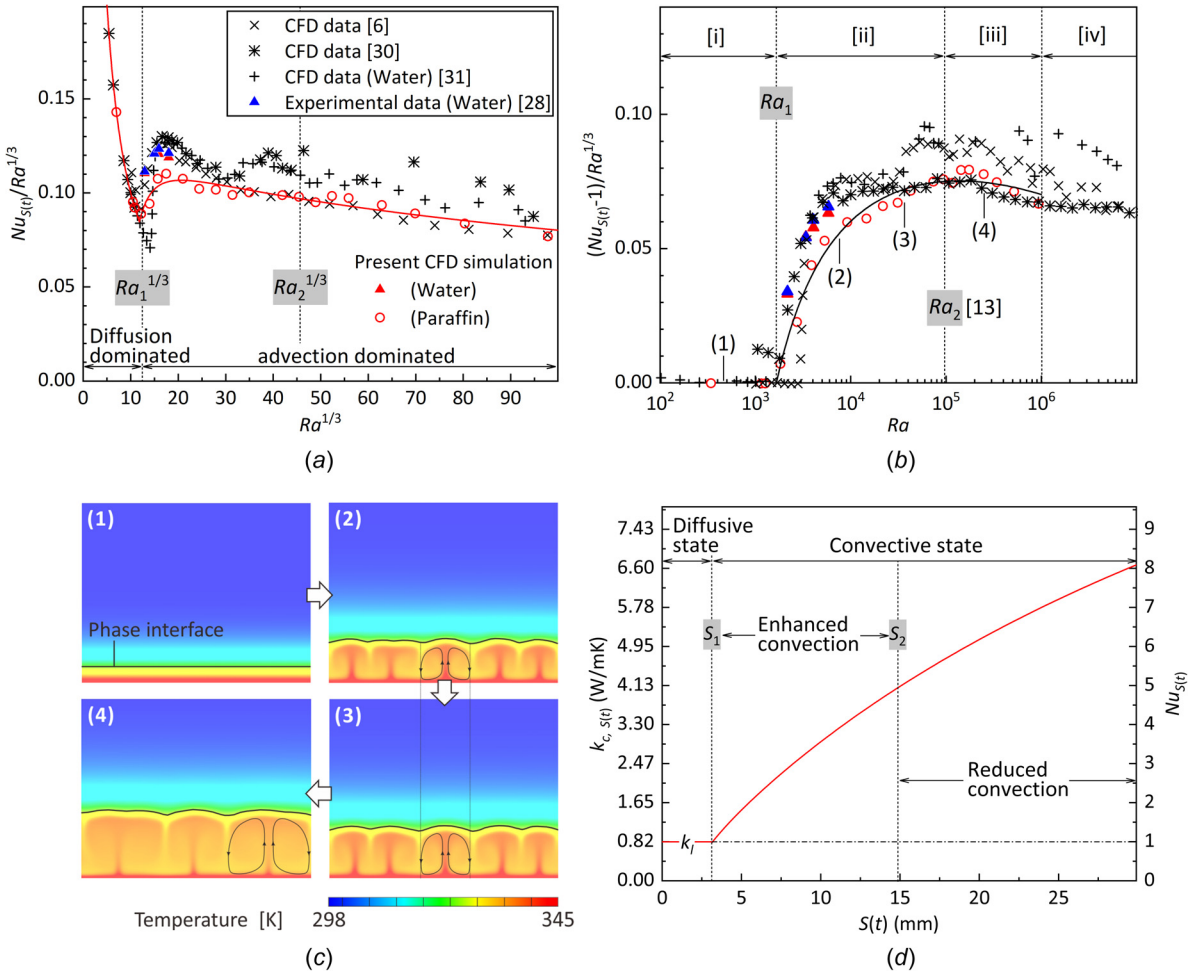

Fig. 7 Quasi-steady-state variations. (*a*) Nondimensional comparisons of the convective constituent ($Nu/Ra^{1/3}$) with respect to the melt layer thickness in $Ra^{1/3}$. (*b*) Nondimensional comparisons of the advective constituent ($(Nu-1)/Ra^{1/3}$) with respect to the melt layer thickness in Ra. (*c*) Numerical melting process at different times (1) $t = 50$ s, (2) $t = 250$ s, (3) $t = 300$ s, and (4) $t = 650$ s for the temperature field. (*d*) Correlated "convective conductivity" ($k_{c,S(t)}$) and Nusselt number ($Nu_{S(t)}$) as a function of the melt's depth ($S(t)$) in Eq. (17).

"convective conductivity." The convective conductivity ($k_{c,S(t)}$) was defined as

$$k_{c,S(t)} = h_{c,S(t)} S(t) \tag{14}$$

where $h_{c,S(t)}$ is the convective heat transfer coefficient that is a quantitative measure of R–B convection, varying with the time dependent melt layer thickness, $S(t)$. We further assumed the thermophysical properties of the PCM to be both thermally and temporally invariant for the two distinct phases and the thermal expansion of the two phases to be negligible [33].

In previous studies [6,29,30], the steady-state dependence of convective heat transfer, $h_{c,S(t)} = q''_{\text{Conv}}/(T_w - T_m)$ on the thickness of a liquid layer, $S(t)$ has already been evaluated in a nondimensional form as $\text{Nu}_{s(t)}/\text{Ra}^{1/3}$ versus $\text{Ra}^{1/3}$ as plotted in Fig. 7(*a*). Here, q''_{Conv} is the total net input (convective) heat flux, $\text{Nu}_{S(t)} = h_{c,S(t)} S(t)/k_l$ and $\text{Ra} = \rho_l g c_{pl} \beta_l (T_w - T_m) S^3(t)/\nu_l k_l$, where g is the gravitational acceleration, ρ_l, c_{pl}, β_l, and ν_l are the density, thermal capacity, thermal expansion coefficient, and kinematic viscosity of a liquid PCM, respectively.

Referring to Fig. 7(*a*), the parameter $\text{Ra}^{1/3}$ represents the thickness of the liquid layer (i.e., $\sim S(t)$) with other parameters invariant. When $\text{Ra}^{1/3}$ initially increases ($\text{Ra}^{1/3} < 12$), the parameter $\text{Nu}_{s(t)}/\text{Ra}^{1/3}$ decreases steeply as the liquid layer thickens, which indicates that heat transfer from the planar isothermal boundary (i.e., $\sim h_{c,S(t)}$), $\text{Nu}_{s(t)}/\text{Ra}^{1/3} \sim 1/\text{Ra}^{1/3}$ (i.e., $h_{c,S(t)} \sim 1/S(t)$). Based on Fourier's law ($k_l/S(t) = q''_{\text{Cond}}/(T_w - T_m)$) and energy balance, ($q''_{\text{Conv}} = q''_{\text{Cond}}$), $h_{c,S(t)} = k_l/S(t)$ can be obtained to represent the variation of the convective heat transfer coefficient with the liquid layer's thickness. This indicates that diffusion dominates within $\text{Ra}^{1/3} \leq 12$.

After R–B convection becomes significant ($\text{Ra}^{1/3} > 12$), the convective heat transfer coefficient contributed by diffusion continues to decrease while advection becomes apparent. For the co-existence of diffusion and advection, the overall convective heat transfer coefficient increases and yet turns to gradually decreases (Fig. 7(*a*)) [6,28,30,31]. For confirmation, a series of independent numerical simulations were performed using identical conditions to the present experiments with a paraffin wax (Sec. 3). Results are compared in Fig. 7(*a*), showing excellent agreement with existing steady-state CFD simulations [6,28,30,31] and with existing experimental data with water [28].

The convective heat transfer coefficient ($h_{c,S(t)}$) can now be expressed as a function of the melt thickness, $S(t)$, by a piecewise function as

$$h_{c,S(t)} = \begin{cases} \dfrac{k_l}{S(t)}, & 0 \leq S(t) \leq S_1 \\ \dfrac{k_l}{S(t)} + h_{a,S(t)}, & S_1 < S(t) \end{cases} \tag{15}$$

This formulation implies that for any arbitrary $S(t)$, more heat is transferred across the melt layer by R–B convection (i.e., advection).

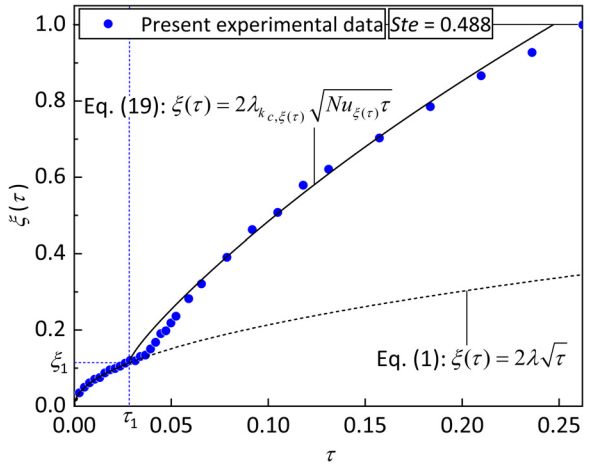

Fig. 8 The temporal progression of the melting front with Rayleigh–Bénard convection predicted by our extended Neumann's solution, Eq. (19) compared with our experimental data for Ste = 0.488

The critical depth at which Rayleigh–Bénard convection becomes significant was found to be $S(t) = S_1 = 3.17$ mm based on our CFD simulations. Here, we define the advective heat transfer coefficient ($h_{a,S(t)}$) as a function of the melt layer thickness being fitted based on the present CFD data as

$$h_{a,S(t)} = \frac{S(t) - S_1}{C_1 + C_2[S(t) - S_1] + C_3[S(t) - S_1]^2} \tag{16}$$

where C_1, C_2, and C_3 are constants depending on material properties and experimental conditions [34]. These constants were determined as $C_1 = 7.54 \times 10^{-6}$ m^{3}K/W, $C_2 = 3.22 \times 10^{-3}$ m^{2}K/W, and $C_3 = 6.03 \times 10^{-2}$ mK/W.

Referring to Fig. 7(*b*), the parameter $(\mathrm{Nu}_{s(t)} - 1)/\mathrm{Ra}^{1/3}$ represents the nondimensional advective heat transfer coefficient, four distinguishable states are shown in Fig. 7(*b*) as follows: [i] diffusive state, [ii] enhanced advective state, [iii] reduced advective state, and [iv] turbulent state.

As claimed before, in the diffusive state, conduction dominates ($\mathrm{Ra} < 1728$) with no apparent advective motion in the melt (Fig. 7(*c*) (1)). The advective heat transfer coefficient remains 0. After R–B convection becomes significant ($\mathrm{Ra} > 1728$), it changes to the convective state which contains the enhanced advective state and the reduced advective state. In the enhanced advective state, the plumes lengthen vertically and the horizontal width of the Bénard cells is fixed while the average fluid thickness continues to increase with time and a clearly nonplanar interface is formed (Fig. 7(*c*) (2, 3)) [6]. The advective heat transfer coefficient increases as the melt layer thickens, and this state ends at $\mathrm{Ra} = 10^5$ [13]. As the melting progresses further, the Bénard cells become vertically elongated until they become stable again, and then a new set of cells is generated by the instability, with a larger horizontal cell width (Fig. 7(*c*) (4)) [6]. As the width of the Bénard cell increases, the cell number decreases and the heat exchange decreases [36]. Therefore, the advective heat transfer coefficient decreases as the melt thickness increases after the peak as depicted in Fig. 7(*b*).

Substitution of Eqs. (15) and (16) into Eq. (14) yields the "convective conductivity" in a piecewise function

$$k_{c,S(t)} = \begin{cases} k_l, & 0 \le S(t) \le S_1 \\ k_l + \dfrac{[S(t) - S_1]S(t)}{C_1 + C_2[S(t) - S_1] + C_3[S(t) - S_1]^2}, & S_1 < S(t) \end{cases} \tag{17}$$

Subsequently, the nondimensional heat transfer coefficient, Nusselt number was expressed as

$$\mathrm{Nu}_{S(t)} = \frac{h_{c,S(t)}S(t)}{k_l} = \frac{k_{c,S(t)}}{k_l} = \begin{cases} 1, & 0 \le S(t) \le S_1 \\ 1 + \dfrac{[S(t) - S_1]S(t)}{k_l\left\{C_1 + C_2[S(t) - S_1] + C_3[S(t) - S_1]^2\right\}}, & S_1 < S(t) \end{cases} \tag{18}$$

Two distinctive states by R–B convection are indicated in Fig. 7(*d*). At the diffusive state ($S(t) < S_1$), diffusion dominates, i.e., $k_{c,S(t)} = k_l$. Thus, the Nusselt number is equal to 1.0. At $S(t) \ge S_1$, advection by R–B cells becomes dominant as shown by Fig. 7(*d*), termed "convective state." Thus, more heat is transferred causing the convective conductivity and the Nusselt number to increase.

Now, the terms of k_l and λ in the original Neumann's solution of Eq. (1*a*) are replaced by "convective conductivity" $k_{c,S(t)}$ and $\lambda_{kc,S(t)}$ where the corresponding $\lambda_{kc,S(t)}$ can be solved from the transcendental equation (Eq. (2)). Finally, our extended Neumann's solution that implicitly includes R–B convection's effect is expressed in the dimensional form as

$$S(t) = 2\lambda_{kc,S(t)}\sqrt{\frac{k_{c,S(t)}t}{\rho_l c p_l}} = 2\lambda_{kc,S(t)}\sqrt{\frac{k_{c,S(t)}k_l t}{k_l \rho_l c p_l}} = 2\lambda_{kc,S(t)}\sqrt{\frac{\mathrm{Nu}_{S(t)}k_l t}{\rho_l c p_l}} \tag{19a}$$

Similar to Neumann's solution (Eq. (1*b*)), the extended Neumann's solution has a dimensionless form as

$$\xi(\tau) = 2\lambda_{kc,\xi(\tau)}\sqrt{\mathrm{Nu}_{\xi(\tau)}\tau} \tag{19b}$$

where

$$\mathrm{Nu}_{\xi(\tau)} = \begin{cases} 1, & 0 \le \xi(\tau) \le \xi_1 \\ 1 + \dfrac{[\xi(\tau) - \xi_1]\xi(\tau)}{k_l\left\{C_1/H^2 + C_2[\xi(\tau) - \xi_1]/H + C_3[\xi(\tau) - \xi_1]^2\right\}}, & \xi_1 < \xi(\tau) \end{cases}$$

$\xi_1 = S_1/H$, and $\lambda_{kc,\xi(\tau)}$ is the positive root of the transcendental equation (Eq. (2)) with the nondimensional thickness (Appendices A).

4.2 The Extended Neumann's Solution. By solving our extended Neumann's solution (Eq. (19)), the temporal progression of the liquid–solid interface (or melting front) can be estimated. Results in Fig. 8 show that the melting front initially moves away from the isothermal planar surface as predicted by Neumann's solution. In this diffusive state ($\tau \leq \tau_1$), diffusion dominates albeit R–B cells are present. Our experimental data points follow Neumann's solution perfectly. After the critical time τ_1 (or thickness ξ_1) beginning the convective state, R–B convection becomes dominant—the co-existence of diffusion and advection. Therefore, the measured melting front moves faster than Neumann's solution as expected. As time elapses, the deviation becomes significant, which proves the inapplicability of Neumann's solution with R–B convection.

Our extended Neumann's solution, which is based on a series of the numerical simulations that are independent of the present experiments shows good agreement with subtle yet acceptable differences. These differences include the critical melting time predicted by our CFD simulation occurring earlier than that in the experiments. This may be because at the precise of moment of the R–B convection dominance, the velocity of the melting front increases steeply and thus it cannot be accurately captured experimentally. Further, the full melting time measured is slightly slower due to the heat loss near the top boundary of the container used in the experiment.

Nonetheless, the good prediction by the extended Neumann's solution suggests that nondiffusion dominant constituents like R–B convection in the melt layer alter only the melt layer's equivalent thermal conductivity as a sole mechanism for transferring heat across the stratified liquid–solid material. Thus, the "stagnant thermal" conductivity in Neumann's solution is replaced with lumped "convective conductivity." Now the distinctive temporal thickening contribution of the melt layer is incorporated into Neumann's solution that addresses the presently perceived inapplicability. With the new semi-analytically extended Neumann's solution, it is possible to now estimate the temporal, countergravitational progression of a liquid–solid interface with R–B convection in a typical phase change material.

5 Conclusions

Neumann's solution accurately predicts the melting front propagation, for diffusion dominated heat transfer through the PCM, which occurs when the constant temperature wall is located above the PCM and the liquid–solid interface moves downward along the gravitational axis. On the other hand, placement of the constant temperature wall below the PCM, results in the melting front moving in the direction opposed to the gravitational axis. This condition is associated with the onset of R–B convection and the classical Neumann's solution is inapplicable. We proposed a semi-analytical model that extended Neumann's solution to predict the temporal, countergravitational progression of a liquid–solid interface with R–B convection in a typical phase change material. The model incorporated a lumped parameter, "time-dependent convective conductivity" with Neumann's solution. The extension was implicit and semi-analytical. The precise prediction by the extended Neumann's solution clearly demonstrated that nondiffusion dominant constituents like R–B convection in the melt layer alter only its equivalent thermal conductivity as a sole mechanism for transferring heat across the stratified liquid–solid material.

Despite demonstrating the applicability of the extended Neumann's solution when there is R–B convection, the following limitations of the approach need to be noted:

(1) The thermal-physical properties of phase change materials should not vary dramatically with temperature, as constant thermal-physical properties were assumed in the analysis.
(2) The thermal expansion should be relatively small, since the thermal expansion of the two phases was assumed to be negligible.
(3) The thermal conductivity of phase change materials should be relatively small, since the melting process was assumed to be quasi-steady.
(4) Laminar Rayleigh–Bernard convection was assumed. Thus, the present extended semi-analytical model is only applicable for the Rayleigh numbers lower than, e.g., $\mathrm{Ra} = 1.0 \times 10^6$.

The extended Neumann's solution can be applied to predict the variation of the liquid–solid interface over time under the influence of Rayleigh–Bernard convection, and thus used to design and optimize phase change energy storage systems.

Acknowledgment

We thank Ms. Ziyi Gu for her assistance in setting up our experiments and performing the measurements.

Funding Data

- The State Key Laboratory of Mechanics and Control for Aerospace Structures (MCMS-E-0219 K02).
- China, Double Innovation Talent Foundation of Jiangsu Province (JSSCRC2021502).
- National Natural Science Foundation of China (Grant No. 12032010; Funder ID: 10.13039/501100001809)
- China, and Ministry of Science and ICT of Korea via the National Research Foundation of Korea (Grant No. 2021R1A2C3007705; Funder ID: 10.13039/501100003725).

Data Availability Statement

The datasets generated and supporting the findings of this article are obtainable from the corresponding author upon reasonable request.

Nomenclature

c_p = thermal capacity, J/kg K
D_h = hydraulic diameter, m
g = gravitational acceleration, m/s^2
H = total thickness of the melt layer, m
h_a = advective heat transfer coefficient, W/m^2 K
h_c = convective heat transfer coefficient, W/m^2 K
k = thermal conductivity, W/m K
$k_{c,S(t)}$ = convective conductivity, W/m K
L = length of the test section, m
L_e = length of the developing regime, m
L_h = latent heat, J/kg
N = solid-to-liquid ratio
Nu = Nusselt number
q'' = heat flux, W/m^2
Ra = Rayleigh number
Re_{Dh} = Reynolds number
S = melt layer thickness, m
Ste = Stefan number
t = melt time, s
T_m = melting temperature, K
T_r = reference temperature, K
T_w = isothermal wall temperature, K
T_0 = initial temperature, K
U_m = mean velocity, m/s
$U_{\mathrm{max,\ R–B}}$ = maximum velocity magnitude of the R–B convection, m/s
W = width of the test section, m

Greek Symbols

α = thermal diffusivity, m^2/s
β = coefficient of thermal expansion, 1/K

δ = thickness of the shaded area, m
λ = positive root of the transcendental equation
μ = dynamic viscosity, Pa·s
ν = kinematic viscosity, m^2/s
ξ = dimensionless melt thickness
ρ = density, kg/m^3
σ = deviation
τ = dimensionless melt time

Subscripts

cond = conduction
conv = convection
l = liquid
max = maximum
min = minimum
s = solid

Abbreviations

PCM = phase change material
R–B = Rayleigh–Bénard

Appendix A: Derivation of Extended Neumann's Solution for Quasi-Steady State Phase Transition

Here, we present a full derivation of our extension for Neumann's solution. For a typical PCM in thermal energy storage applications, e.g., paraffin, the phase transition occurs quasi-steadily due to the intrinsically low stagnant thermal conductivity [32]. We incorporated a lumped parameter that accounted for heat transfer across the melt (or liquid) layer solely via equivalent conduction, newly termed "convective conductivity."

The convective conductivity ($k_{c,S(t)}$) was defined as

$$k_{c,S(t)} = h_{c,S(t)}S(t) \tag{A1}$$

where $h_{c,S(t)}$ is the convective heat transfer coefficient that varies with the time dependent melt layer thickness, $S(t)$. We further assumed the thermal and temporal invariances in the physical properties of the two distinct phases and ignored thermal expansion of the two phases, i.e., invariant density and volume [33].

By assuming very slow phase transition (i.e., quasi-steady-state phase transition), a series of steady-state numerical simulations were carried out using a commercial program, where the melted layer thickness (S) was varied, and the convective heat transfer coefficient determined. Thus, the convective heat transfer coefficient ($h_{c,S(t)}$) can be fitted by a piecewise function as

$$h_{c,S(t)} = \begin{cases} \dfrac{k_l}{S(t)}, & 0 \le S(t) \le S_1 \\ \dfrac{k_l}{S(t)} + h_{a,S(t)}, & S_1 < S(t) \end{cases} \tag{A2}$$

This formulation implies that for any arbitrary $S(t)$, more heat is transferred across the melt layer by R–B convection (i.e., advection). The critical depth at which Rayleigh–Bénard convection becomes significant was found to be $S(t) = S_1 = 3.17$ mm based on our CFD simulations. Here, we define the advective heat transfer coefficient ($h_{a,S(t)}$) as a function of the *quasi-steady* melt layer thickness, being fitted based on the present CFD data as

$$h_{a,S(t)} = \frac{S(t) - S_1}{C_1 + C_2[S(t) - S_1] + C_3[S(t) - S_1]^2} \tag{A3}$$

where C_1, C_2, and C_3 are constants depending on material properties and experimental conditions [33]. These constants were determined as $C_1 = 7.54 \times 10^{-6}$ m^3K/W, $C_2 = 3.22 \times 10^{-3}$ m^2K/W, and $C_3 = 6.03 \times 10^{-2}$ mK/W. Here, we use a commercial software Origin 2018 to fit with the Rational-Nelder model [36] for a confidence interval of 0.974.

Substitution of Eqs. (A2) and (A3) into Eq. (A1) yields the "convective conductivity" in a piecewise function

$$k_{c,S(t)} = \begin{cases} k_l, & 0 \le S(t) \le S_1 \\ k_l + \dfrac{[S(t) - S_1]S(t)}{C_1 + C_2[S(t) - S_1] + C_3[S(t) - S_1]^2}, & S_1 < S(t) \end{cases} \tag{A4}$$

Subsequently, the nondimensional parameter, Nusselt number is derived as

$$\mathrm{Nu}_{S(t)} = \frac{h_{c,S(t)}S(t)}{k_l} = \frac{k_{c,S(t)}}{k_l} = \begin{cases} 1, & 0 \le S(t) \le S_1 \\ 1 + \dfrac{[S(t) - S_1]S(t)}{k_l\left\{C_1 + C_2[S(t) - S_1] + C_3[S(t) - S_1]^2\right\}}, & S_1 < S(t) \end{cases} \tag{A5}$$

Now, the terms of k_l and λ in Neumann's solution, Eq. (1*a*) is replaced by "convective conductivity" $k_{c,S(t)}$ and $\lambda_{kc,S(t)}$ where the corresponding $\lambda_{kc,S(t)}$ can be solved from the transcendental equation (Eq. (2)). Finally, our extended Neumann's solution that implicitly includes R–B convection's effect is expressed in the dimensional form (Fig. 9(*a*)) as

$$S(t) = 2\lambda_{kc,S(t)}\sqrt{\frac{k_{c,S(t)}t}{\rho_l c_{pl}}} = 2\lambda_{kc,S(t)}\sqrt{\frac{k_{c,S(t)}k_l t}{k_l\rho_l c_{pl}}} = 2\lambda_{kc,S(t)}\sqrt{\frac{\mathrm{Nu}_{S(t)}k_l t}{\rho_l c_{pl}}} \tag{A6}$$

where $\lambda_{kc,S(t)}$ is the positive root of the following transcendental equation (2), where N_k and N_α are the solid-to-liquid with "convective conductivity" ratios of conductivity to ($k_s/k_{c,S(t)}$) and diffusivity ($k_s\rho_l c_{pl}/k_{c,S(t)}\rho_s c_{ps}$), respectively. Thus, the λ is a function of $k_{c,S(t)}$, i.e., $\lambda_{kc,S(t)}$, the corresponding $\lambda_{kc,S(t)}$ can be solved from the transcendental equation (Eq. (2)) under each k_c within the range of $k_c = 0.825$–6.68, by fitting, we obtain a correlation

$$\lambda_{kc,S(t)} = E_0 + E_1 k_{c,S(t)} + E_2 k_{c,S(t)}^2 + E_3 k_{c,S(t)}^3 + E_4 k_{c,S(t)}^4 + E_5 k_{c,S(t)}^5 \tag{A7}$$

where $E_0 = 3.1587 \times 10^{-1}$, $E_1 = 3.712 \times 10^{-2}$ mK/W, $E_2 = -1.522 \times 10^{-2}$ m^2K^2/W^2, $E_3 = 3.38 \times 10^{-3}$ m^3K^3/W^3, $E_4 = -3.78514 \times 10^{-4}$ m^4K^4/W^4, and $E_5 = 1.67548 \times 10^{-5}$ m^5K^5/W^5.

Using the same nondimensionalization as Neumann's solution, $\xi = S(t)/H$ and $\tau = \alpha_l t/H^2$, the convective heat transfer coefficient, "convective conductivity" and Nusselt number vary with nondimensional thickness and time have such forms

$$h_{c,\xi(\tau)} = \begin{cases} \dfrac{k_l}{H\xi(t)}, & 0 \le \xi(\tau) \le \xi_1 \\ \dfrac{k_l}{H\xi(t)} + \dfrac{\xi(\tau) - \xi_1}{C_1/H + C_2[\xi(\tau) - \xi_1] + C_3 H[\xi(\tau) - \xi_1]^2}, & \xi_1 < \xi(\tau) \end{cases} \tag{A8}$$

$$k_{c,\xi(\tau)} = \begin{cases} k_l, & 0 \le \xi(\tau) \le \xi_1 \\ k_l + \dfrac{[\xi(\tau) - \xi_1]\xi(\tau)}{C_1/H^2 + C_2[\xi(\tau) - \xi_1]/H + C_3[\xi(\tau) - \xi_1]^2}, & \xi_1 < \xi(\tau) \end{cases} \tag{A9}$$

$$\mathrm{Nu}_{\xi(\tau)} = \begin{cases} 1, & 0 \le \xi(\tau) \le \xi_1 \\ 1 + \dfrac{[\xi(\tau) - \xi_1]\xi(\tau)}{k_l\left\{C_1/H^2 + C_2[\xi(\tau) - \xi_1]/H + C_3[\xi(\tau) - \xi_1]^2\right\}}, & \xi_1 < \xi(\tau) \end{cases} \tag{A10}$$

where $\xi_1 = S_1/H$.

Then, our extension for Neumann's solution has a dimensionless form

$$\xi(\tau) = 2\lambda_{kc,\xi(\tau)}\sqrt{\mathrm{Nu}_{\xi(\tau)}\tau} \tag{A11}$$

where

$$\lambda_{kc,\xi(\tau)} = E_0 + E_1 k_{c,\xi(\tau)} + E_2 k_{c,\xi(\tau)}^2 + E_3 k_{c,\xi(\tau)}^3 + E_4 k_{c,\xi(\tau)}^4 + E_5 k_{c,\xi(\tau)}^5 \tag{A12}$$

Now, we justify the quasi-steady-state assumption which states that phase transition takes place at a slow rate. We obtain the melt front velocity, which changes with melting time, and analyze whether the quasi-steady assumption can be used.

Equation (A6) can be changed to

$$t = \frac{S^2(t)\rho_l c p_l}{4k_{c,S(t)}\lambda_{k_{c,S(t)}}^2} \tag{A13}$$

The melt time, t is used to derive the melt thickness, $S(t)$

$$\frac{dt}{dS(t)} = \frac{\rho_l c p_l}{4}\frac{S(t)\left(2k_{c,S(t)}\lambda_{kc,S(t)} - S(t)\lambda_{kc,S(t)}\dfrac{dk_{c,S(t)}}{dS(t)} - 2S(t)k_{c,S(t)}\dfrac{d\lambda_{kc,S(t)}}{dk_{c,S(t)}}\dfrac{dk_{c,S(t)}}{dS(t)}\right)}{k_{c,S(t)}^2\lambda_{k_{c,S(t)}}^3} \tag{A14}$$

where

$$\frac{d\lambda_{kc,S(t)}}{dk_{c,S(t)}} = E_1 + 2E_2 k_{c,S(t)} + 3E_3 k_{c,S(t)}^2 + 4E_4 k_{c,S(t)}^3 + 5E_5 k_{c,S(t)}^4 \tag{A15}$$

$$\frac{dk_{c,S(t)}}{dS(t)} = \begin{cases} 0, & 0 \le S(t) \le S_1 \\ \dfrac{C_1 S_1 + 2C_1[S(t) - S_1] + (C_2 - C_3 S_1)[S(t) - S_1]^2}{\left\{C_1 + C_2[S(t) - S_1] + C_3[S(t) - S_1]^2\right\}^2}, & S_1 < S(t) \end{cases} \tag{A16}$$

Thus, the velocity of the melt front can be expressed as

$$\frac{dS(t)}{dt} = \frac{4}{\rho_l c p_l}\frac{k_{c,S(t)}^2\lambda_{k_{c,S(t)}}^3}{S(t)\left(2k_{c,S(t)}\lambda_{kc,S(t)} - S(t)\lambda_{kc,S(t)}\dfrac{dk_{c,S(t)}}{dS(t)} - 2S(t)k_{c,S(t)}\dfrac{d\lambda_{kc,S(t)}}{dk_{c,S(t)}}\dfrac{dk_{c,S(t)}}{dS(t)}\right)} \tag{A17}$$

By solving Eq. (A17) and our extended Neumann's solution Eq. (A6), the relationship between the melt front velocity and time is obtained (Fig. 9(*b*)). Although the melt thickness is time-dependent, the melt velocity is small enough less than 1.5×10^{-4} m/s. The quasi-steady-state assumption can further be justified by the melting front velocity (dS/dt) with respect to the maximum velocity magnitude of the R–B convection (i.e., fluid motion) ($U_{\max,\,\mathrm{R–B}}$) obtained from the present CFD simulations. The result depicted in Fig. 9(*c*) shows that overall the phase transition takes place at much slower rates in comparison to the convective fluid motion. The fastest phase transition occurs at the onset of convective state being $(dS/dt)/(U_{\max,\,\mathrm{R–B}}) \sim 0.031$, followed by a dramatic decrease as the melt layer thickens. Consequently, the quasi-steady-state phase transition may be justified. Therefore, the convective heat transfer coefficient can be considered as a function of the melt thickness only, in turn, allowing the quasi-steady-state assumption in the analysis.

Appendix B: Melting With R–B Convection

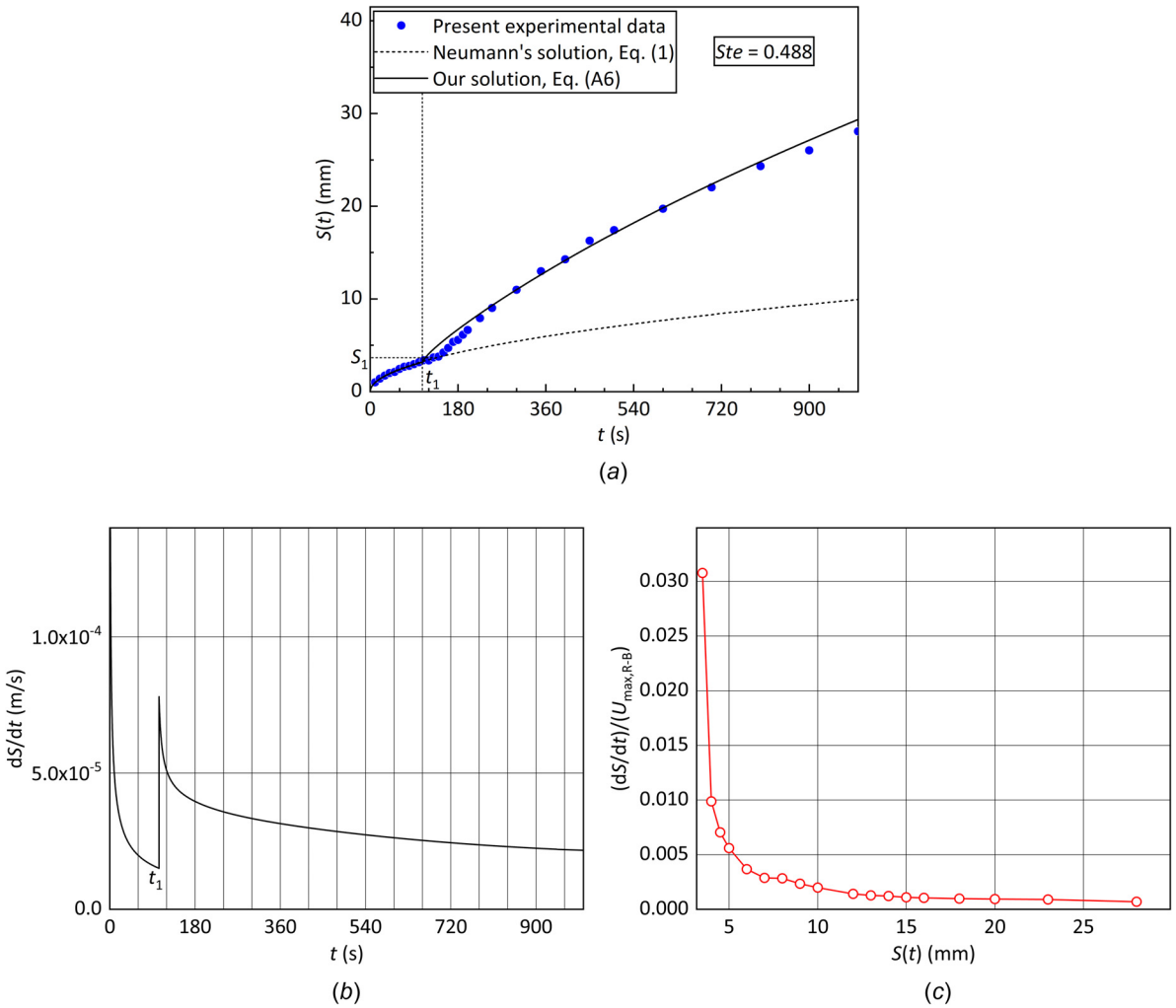

Fig. 9 Melting with R–B convection. (*a*) The temporal progression of the melting front with Rayleigh–Bénard convection predicted by our extended Neumann's solution, Eq. (A6) compared with our experimental data for Ste = 0.488. (*b*) Quasi-steady state variation of the melting front velocity (*dS*/*dt*) with respect to the melting time (*t*). (*c*) The melting front velocity (*dS*/*dt*) relative to the maximum velocity magnitude of R–B convection ($U_{max,\ R-B}$) obtained from the present CFD simulations.

References

[1] Woods, J., Mahvi, A., Goyal, A., Kozubal, E., Odukomaiya, A., and Jackson, R., 2021, "Rate Capability and Ragone Plots for Phase Change Thermal Energy Storage," Nat. Energy, **6**(3), pp. 295–302.

[2] Stefan, J., 1891, "Über Die Theorie Der Eisbildung, Insbesondere Über Die Eisbildung im Polarmeere," Ann. Phys., **278**(2), pp. 269–286.

[3] Gau, C., and Viskanta, R., 1984, "Melting and Solidification of a Metal System in a Rectangular Cavity," Int. J. Heat Mass Transfer, **27**(1), pp. 113–123.

[4] Madruga, S., Haruki, N., and Horibe, A., 2018, "Experimental and Numerical Study of Melting of the Phase Change Material Tetracosane," Int. Commun. Heat Mass Transfer, **98**, pp. 163–170.

[5] Carslaw, H. S., and Jaeger, J. C., 1959, *Conduction of Heat in Solids*, Oxford University Press, New York, Chap. 6.

[6] Favier, B., Purseed, J., and Duchemin, L., 2019, "Rayleigh–Bénard Convection With a Melting Boundary," J. Fluid Mech., **858**, pp. 437–473.

[7] Boger, D. V., and Westwater, J. W., 1967, "Effect of Buoyancy on the Melting and Freezing Process," ASME J. Heat Mass Transfer-Trans. ASME, **89**(1), pp. 81–89.

[8] Yen, Y. C., 1968, "Onset of Convection in a Layer of Water Formed by Melting Ice From Below," Phys. Fluids, **11**(6), pp. 1263–1270.

[9] Hale, N. W., Jr., and Viskanta, R., 1980, "Solid-Liquid Phase-Change Heat Transfer and Interface Motion in Materials Cooled or Heated From Above or Below," Int. J. Heat Mass Transfer, **23**(3), pp. 283–292.

[10] Gau, C., and Viskanta, R., 1985, "Effect of Natural Convection on Solidification From Above and Melting From Below of a Pure Metal," Int. J. Heat Mass Transfer, **28**(3), pp. 573–587.

[11] Gong, Z. X., and Mujumdar, A. S., 1998, "Flow and Heat Transfer in Convection-Dominated Melting in a Rectangular Cavity Heated From Below," Int. J. Heat Mass Transfer, **41**(17), pp. 2573–2580.

[12] Kousksou, T., Arid, A., Majid, J., and Zeraouli, Y., 2010, "Numerical Modeling of Double-Diffusive Convection in Ice Slurry Storage Tank," Int. J. Refrig., **33**(8), pp. 1550–1558.

[13] Madruga, S., and Curbelo, J., 2018, "Dynamic of Plumes and Scaling During the Melting of a Phase Change Material Heated From Below," Int. J. Heat Mass Transfer, **126**, pp. 206–220.

[14] Duan, J., Xiong, Y., and Yang, D., 2019, "On the Melting Process of the Phase Change Material in Horizontal Rectangular Enclosures," Energies, **12**(16), p. 3100.

[15] Guo, W., Zhao, R., Liu, Y., and Huang, D., 2021, "Semi-Theoretical Correlations of Melting Process Driven by Rayleigh–Bénard Convection Suitable for Low Melting Point Metal," Case Stud. Therm. Eng., **28**, p. 101511.

[16] Farid, M. M., and Mohamed, A. K., 1987, "Effect of Natural Convection on the Process of Melting and Solidification of Paraffin Wax," Chem. Eng. Commun., **57**(1–6), pp. 297–316.

[17] Du, X. Z., Yang, Z. G., Jin, Z. Y., Xia, C., and Bao, D., 2018, "A Comparative Study of Passive Control on Flow Structure Evolution and Convective Heat Transfer Enhancement for Impinging Jet," Int. J. Heat Mass Transfer, **126**, pp. 256–280.

[18] Koşan, M., and Şahin, H. M., 2017, "Numerical Analysis of a Heat Exchanger in a Thermal Energy Storage System," Proceedings of the 23rd International Conference on Engineering, Technology and Innovation, Madeira, Portugal, June 27–29, pp. 1–9.

[19] Hussein, H. A., Abed, A. H., and Abdulmunem, A. R., 2016, "An Experimental Investigation of Using Aluminum Foam Matrix Integrated With Paraffin Wax as a Thermal Storage Material in a Solar Heater," Proceeding of the 2nd Sustainable and Renewable Energy Conference, Baghdad, Iraq, Nov. 26–27, Paper No. ASE-6.
[20] Buonomo, B., Ercole, D., Manca, O., and Nardini, S., 2017, "Numerical Investigation on Thermal Behaviors of Two-Dimensional Latent Thermal Energy Storage With PCM and Aluminum Foam," J. Phys.: Conf. Ser., **796**, p. 012031.
[21] Shi, X., Bin, Y., Hou, D., Men, Y., and Matsuo, M., 2014, "Gelation/Crystallization Mechanisms of UHMWPE Solutions and Structures of Ultradrawn Gel Films," Polym. J., **46**(1), pp. 21–35.
[22] Tse, C. C. W., Ng, S. S., Stringer, J., MacNeil, S., Haycock, J. W., and Smith, P. J., 2016, "Utilising Inkjet Printed Paraffin Wax for Cell Patterning Applications," Int. J. Bioprint., **2**, pp. 35–44.
[23] Alade, O. S., Hassan, A., Mahmoud, M., Al-Shehri, D., and Al-Majed, A., 2020, "Novel Approach for Improving the Flow of Waxy Crude Oil Using Thermochemical Fluids: Experimental and Simulation Study," ACS Omega, **5**(8), pp. 4313–4321.
[24] Mohanty, S., and Arora, R., 2020, "CFD Analysis of a Shell and Tube Heat Exchanger With Single Segmental Baffles," Int. J. Automot. Mech. Eng., **17**(2), pp. 7890–7901.
[25] Bucio, A., Moreno-Tovar, R., Bucio, L., Espinosa-Dávila, J., and Anguebes-Franceschi, F., 2021, "Characterization of Beeswax, Candelilla Wax and Paraffin Wax for Coating Cheeses," Coatings, **11**(3), p. 261.
[26] Coleman, H. W., and Steele, W. G., 2018, *Experimentation, Validation, and Uncertainty Analysis for Engineers*, Wiley, New York, Chap. 2.
[27] Mukutmoni, D., and Yang, K. T., 1993, "Rayleigh-Bénard Convection in a Small Aspect Ratio Enclosure: Part I—Bifurcation to Oscillatory Convection," ASME J. Heat Mass Transfer-Trans. ASME, **115**(2), pp. 360–366.
[28] Farhadieh, R., and Tankin, R., 1974, "Interferometric Study of Two-Dimensional Bénard Convection Cells," J. Fluid Mech., **66**(4), pp. 739–752.
[29] Wu, Y., and Lacroix, M., 1992, "Numerical Study of a Pure Metal Melting in Presence of Turbulent Natural Convection," Int. J. Numer. Methods Heat Fluid Flow, **2**(3), pp. 235–242.
[30] Esfahani, B. R., Hirata, S. C., Berti, S., and Calzavarini, E., 2018, "Basal Melting Driven by Turbulent Thermal Convection," Phys. Rev. Fluids, **3**(5), p. 053501.
[31] Purseed, J., Favier, B., Duchemin, L., and Hester, E. W., 2020, "Bistability in Rayleigh-Bénard Convection With a Melting Boundary," Phys. Rev. Fluids, **5**(2), p. 023501.
[32] Satbhai, O., and Roy, S., 2020, "Criteria for the Onset of Convection in the Phase-Change Rayleigh–Bénard System With Moving Melting-Boundary," Phys. Fluids, **32**(6), p. 064107.
[33] Prusa, J., and Yao, L. S., 1985, "Effects of Density Change and Subcooling on the Melting of a Solid Around a Horizontal Heated Cylinder," J. Fluid Mech., **155**, pp. 193–212.
[34] Niemela, J. J., Skrbek, L., Sreenivasan, K. R., and Donnelly, R. J., 2000, "Turbulent Convection at Very High Rayleigh Numbers," Nature, **404**(6780), pp. 837–840.
[35] Moon, J. Y., and Chung, B. J., 2019, "Influence of Prandtl Number, Height and Lateral Cooling Condition on Laminar Natural Convection in a Rectangular Enclosure," Heat Mass Transfer, **55**(6), pp. 1593–1605.
[36] OriginLab, 2023, "Help Online - Origin Help—Nelder," OriginLab Corporation, Northampton, MA, accessed May 24, 2023, https://www.originlab.com/doc/en/Origin-Help/Nelder-FitFunc